



Laser welding of tailored blanks made of Al-Si-coated 22MnB5 steel using a filler wire and a variable energy distribution laser optics

Donato Coviello¹ · Jana von der Heydt² · Lorenzo Rullo³ · Michael Keßler² · Mariarosaria De Vito³ · Antonio D'Angola¹ · Donato Sorgente¹

Received: 13 August 2022 / Accepted: 14 January 2023 / Published online: 25 January 2023
© The Author(s) 2023

Abstract

Laser welding of Al-Si-coated steels for hot stamping in automotive applications is problematic due to the mixing of the coating layers inside the molten pool that weakens the resulting weld seam. In this case, the most common welding procedure to overcome this issue consists in removing the Al-Si layer through laser ablation prior to the joining. This method continues to be the most widely used by major producers of tailor welded blanks, although in situ ablation of the Al-Si coating can be costly and time consuming. In this work, a novel approach consisting in joining as-received (i.e., not decoated) materials using a filler wire and an innovative variable energy distribution laser optics is introduced and tested on tailor welded blanks made of 22MnB5. Tensile tests of specimens obtained from a 3³ full factorial design of experiment have shown an average value of ultimate tensile strength of 1523 MPa, which is much higher than the one usually observed in as-received welded then hot-stamped conditions and aligned with hot-stamped base material values. Hardness test results (494–543 HV_{0.5}) were in the typical hot-stamped base material range of values as well, while SEM–EDS analyses detected no ferrite inclusions inside the fusion zone. Variations of the main process parameters have been considered on an iso-thickness and iso-material configuration, empirically demonstrating the stability and reliability of the proposed methodology as well as its suitability for production purposes.

Keywords Tailor welded blanks (TWB) · Al-Si-coated 22MnB5 steel · Laser welding · Press hardened steel · Laser ablation

1 Introduction

In the last decades, automotive manufacturers are facing the very hard challenge to design more and more comfortable and safe cars preserving the vehicle overall weight [1, 2]. Weight reduction is the key factor for the decrease in fuel consumption which is fundamental for all kinds of vehicles, both with internal combustion engines and with electric ones. Indeed, if the former have to satisfy more and more restrictive regulations for environmental pollution and greenhouse gas emissions, the latter have to fully optimize

the energy usage in order to guarantee longer ranges of autonomy per battery charge [3–7]. For these reasons, the development of lightweight solutions for the vehicle body-in-white through the application of both more strength materials and tailored blanks technologies is mandatory nowadays [8–10]. Consequently, the use of advanced high-strength steels (AHSS), and in particular its subfamily of ultra-high-strength steels (UHSS), is growing much more than forecast due to the capability of these grades of steel to reach lightweighting targets without the critical issues of other alternative materials (e.g., aluminum, magnesium, titanium) [11–18]. Typical UHSS problems related to limited formability and significant springback at room temperature have been overcome for press hardened steels (PHS) thanks to hot stamping, which takes advantage of the high formability properties of the austenitic phase at high temperatures [19]. While the as-delivered PHS at room temperature consists of ferrite and pearlite with iron in a body-centered cubic (BCC) lattice, the heating at a temperature between 900 and

✉ Donato Sorgente
donato.sorgente@unibas.it

¹ School of Engineering, Università degli Studi della Basilicata, Via Ateneo Lucano, 10, 85100 Potenza, Italy

² Baosteel Tailored Blanks GmbH, Duisburg, Germany

³ Baosteel Tailored Blanks Srl, Tito Scalo, PZ, Italy

950 °C makes the steel completely austenitized and characterized by a face-centered cubic (FCC) lattice. Finally, the stamping/quenching step ensures the transformation of the steel microstructure into full martensitic one [20]. The use of PHS by carmakers has spread out in the last few years, and the demand will continue to increase according to future forecasts [20]. The most commonly employed PHS is 22MnB5, which is a low-carbon steel grade with manganese and boron alloying. PHS are widely used with an Al-Si coating layer, necessary to protect the austenitized sheet from oxide scale formation and decarburization at the surface during the hot stamping heat treatment [21, 22]. For the optimal exploitation of the lightweight potential of these steel grades, their use as tailored welded blanks (TWB, i.e., two or more sheets of different materials and/or thicknesses joined through a laser beam before stamping) is a viable solution. TWB guarantee also an optimized employment of material usage [23, 24]. However, it is well known that Al-Si coating causes issues in the laser welding process since Al contaminates the molten pool causing the presence of ferrite into the martensite microstructure of the hot-stamped fusion zone (FZ) that weakens the strength of the weld seam [23, 25–29]. Up to now, several different methodologies have been tested in an attempt to solve this problem both with and without the Al-Si layer removal. In industrial applications, the most used method consists in removing the Al-Si coating by means of ablation before welding through a specific Q-switched pulsed laser. This method can preserve efficaciously the underlying Fe-Al intermetallic layer that faces the steel substrate, continuing to guarantee minimum protection of the treated area against oxidation [30]. Nevertheless, the popularity of laser ablation does not imply necessarily that it is the most efficient way to resolve this issue [23]. Generally, coating removal is to be considered not desirable because it entails additional steps and equipment increasing times and costs of the manufacturing process. For these reasons, the latest attempts are all oriented toward methods that avoid ablation as well as any other decoating procedure. Some of these are based on the addition of filler material in the form of a wire inside the FZ [31–35]. The results reported in the literature have shown an effective improvement of the mechanical properties of the joints with filler wire compared to those welded without in hot-stamped condition. The addition of filler wire also allows better control of the weld seam geometry thanks to the possibility to properly adjust the wire feeding speed. It could be noticed that by using filler material, the cost of processing will likely increase due to two main reasons: first, the direct cost of consumables needed for the joining process; and second, the additional capital cost of acquiring the filler wire feeding equipment for the laser welding station. However, these costs result much lower than the capital cost of acquiring and powering the additional laser source for the Al-Si layer ablation. Indeed,

the laser beam properties required by the ablation step are so different from those for the welding process that are impossible to obtain by the same laser source. In other similar approaches, the use of Ni foils as an interlayer between the two sheets to be joined [36–38] or as an additive coating layer on the sheets [39] has been evaluated. Ni is a strong austenite-stabilizer element, acting in this way similarly to carbon filler wire. However, the application of interlayered foils does not allow direct control of the FZ geometry since the variation of thickness of Ni foils has not a significant influence on the shape of welded joints [37]. Moreover, the solution of an additive Ni surface layer, which has been tested only in bead-on-plate tests [39], could be difficult and time-consuming on butt joints for real industrial applications. Other approaches have been developed trying to eliminate the Al-Si layer without a real decoating procedure but through a preheating treatment [40] or the application of a colloidal graphite coating [41, 42]. The former consists in heating the steel sheet prior to laser welding reaching a temperature of 800 °C that allows the evaporation of Al-Si coating but preserves the underlying Fe-Al intermetallic layer [40]. Although it is effective, this method is time-consuming and implies anyway an additional step in the manufacturing process. In addition, the oxidative effects of a preheating treatment of large portions of steel could represent an issue in the following heating for the hot stamping that has not been investigated yet. The latter method uses a colloidal graphite additional coating on the steel that serves both as an austenite stabilizer and an agent for in situ ablation of the molten Al-Si coating. Indeed, the additional coating, having a vaporization temperature higher than Al-Si coating, brings an increase of pressure of the underlying coating that finally explodes. This method is effective for bead-on-plate joints with the highest considered thicknesses of graphite coating [41]. Nevertheless, as already observed before, the application and measurement of a coating thickness in the order of $10^{-4} \div 10^{-5}$ m could be difficult in a real production process with butt joint configuration of different thicknesses sheets. Moreover, the final appearance of the areas adjacent to the weld seam should be investigated since violent spurts of the molten Al-Si coating ejected from the weld pool have been observed with the application of the graphite coating. Other interesting approaches consist in enlarging the laser spot on the workpiece surface through beam defocusing [43], the use of optics with higher focal length [44], with particular beam modules, e.g., collateral dual-beam module [45], or with a laser beam oscillation [46, 47]. In addition, a characteristic Y-shaped weld section, instead of the common X-shaped (or hourglass-shaped) FZ, could be achieved through beam defocusing [43] or setting the process parameters in the narrow range of values that allows to weld in the particular closed (or blind) keyhole condition [48, 49]. Indeed, the weld pool resulting from laser welding with closed keyhole

experiences less fierce flows than the one with open keyhole due to the tighter width of the flow channel around the lower part of the keyhole. This results in a contamination of the weld pool due almost entirely to the top coating and restricted to the upper portion of the FZ [48]. However, the mechanical properties of these kinds of weld in butt joint configuration and hot-stamped conditions, i.e., those of a final TWB press-hardened part, should be better investigated. In this work, a novel patent-pending method for the laser welding of as-received Al-Si-coated PHS combining the use of a characteristic filler wire with an innovative laser beam optic module is presented and evaluated. This original approach is in the running to be a valid alternative to current procedures since it simplifies the entire production process of TWB for hot stamping avoiding any additional decoating step before welding. The reliability of this procedure is tested considering butt joint (i.e., not bead-on-plate) configurations between two metal sheets of the same material and the same thickness. It is important to notice that almost the whole of TWB production for automotive purposes is obtained by the joint of sheets made of different materials and/or with different thicknesses, i.e., with different mechanical responses of the joined parts. Therefore, the evaluation of the strength of a weld seam in an iso-material and iso-thickness butt-welding configuration should be more significant since it represents the most challenging case for the welded joint. The main results of mechanical and chemical investigations of a wide experimental campaign are analyzed in order to find the optimal combination of process parameters. The testing with slight variations of the main process parameters allows to verify the stability of this welding procedure, as well as its suitability to be employed for production purposes. Indeed, little alterations of optimal process parameters due to unexpected events should be borne on production lines without irremediably compromising the weld quality.

Table 2 Specification of cutting and welding laser systems

	Cutting laser	Welding laser
Laser welding source	Trumpf TruDisk 6001 disk laser	Laserline LDF 9000–40 diode laser
Laser wavelength (nm)	1030	900–1080
Beam parameter product, BPP (mm·mrad)	4	40

2 Materials and methods

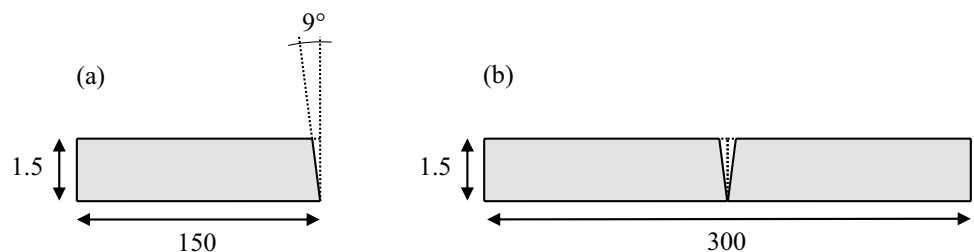
2.1 Materials and specimen preparation

Laser welding tests were carried out on 1.5-mm-thick MBW 1500 PHS steel sheets provided by ThyssenKrupp. This is a 22MnB5 steel coated with an Al-Si protective layer with an average thickness of 30 μm (chemical compositions of both steel and coating in Table 1). Rectangular sheet samples of 220 × 150 mm² were cut on one of the longer sides with a Trumpf TruDisk 6001 disk laser whose beam was oriented to obtain a cut angle of 9° (Fig. 1a). Butt-joint configurations, wherein the laser cut sides were pulled together with no gap (Fig. 1b), were joined with a Laserline LDF 9000–40 diode laser with no shield/assisting gas. The specifications of both cutting and welding lasers are listed in Table 2. The peculiarity of this laser welding process lies in using both a filler wire and an innovative variable energy distribution (VED) optic module. The former is a 1.0-mm-diameter austenite stabilizing filler wire (chemical composition in Table 1) and is fed to the molten pool in front of the laser beam with a feeding angle of 30° and at a feeding height of 1.2 mm from the workpiece surface (Fig. 2). The latter is a multi-spot laser optics (focusing length: 250 mm) that splits the laser beam in an inner circular spot with higher

Table 1 Chemical compositions of base material and protective coating

[Weight %]	C	Mn	Si	S	P	Ni	Cr	Ti	Al	B	Mo	Fe
MBW 1500 base material	0.22	1.28	0.23	0.01	0.01	–	0.23	0.06	0.31	0.005 max	0.01	Bal
Al-Si coating	–	–	11.12	–	–	–	–	–	87.73	–	–	1.14
Filler wire	0.05–0.4	0–3.0	0–2.0	–	–	5–12	4–25	–	–	–	0–0.5	Bal

Fig. 1 Schemes of laser cut on sheet samples (a) and their positioning for laser welding (b) (dimensions in mm)



power densities and an outer squared one with lower power densities (black dashed circle and white dashed square in Fig. 3, respectively). In order to simulate the hot-stamping heat treatment, TWB samples were heated to a temperature of 910 °C for 7 min in a Carbolite Gero CWF 13/65 furnace and quenched for 28 s in a Schütz + Licht ZS1200CN hydraulic press equipped with a room temperature running-water-cooled tool that ensures a cooling rate of 27 °C/s.

2.2 Experimental plan and test procedures

A 3^3 full factorial design of experiment (DoE) was planned centering the plan from a process configuration with the following input data: welding speed v_W of 6 m/min, wire speed v_F of 4 m/min (adimensional ratio $v_W/v_F = 1.5$), laser power P_L of 6.2 kW (heat input $Q = P_L/v_W = 62$ J/mm), and defocusing distance 3.0 mm. This configuration was selected after a preliminary experimental campaign aimed at achieving welds that do not show visual defects, e.g., undercut and concavity of the weld seam. The considered factors for DoE were v_W , v_W/v_F , and Q , while no changes were made on laser defocusing. Table 3 shows the levels considered for each factor for the experimental plan. For each configuration, three replications were made for a total of 81 overall welded samples, and none of them showed macroscopic defects of the weld seam. Tensile specimens with the centered transversal weld seam and dimensions indicated in Fig. 4 were sheared from TWB as-quenched samples and mechanically side-grounded to eliminate any crack starting point. For the comparison between DoE configurations, three tensile tests for each configuration were carried out on an Instron 5982 universal testing machine at a speed of 2 mm/min. Elongation results for DoE comparisons were

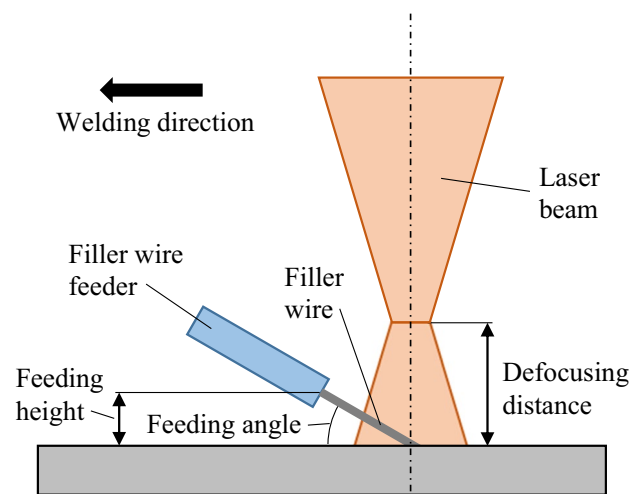


Fig. 2 Scheme of the welding configuration with filler wire

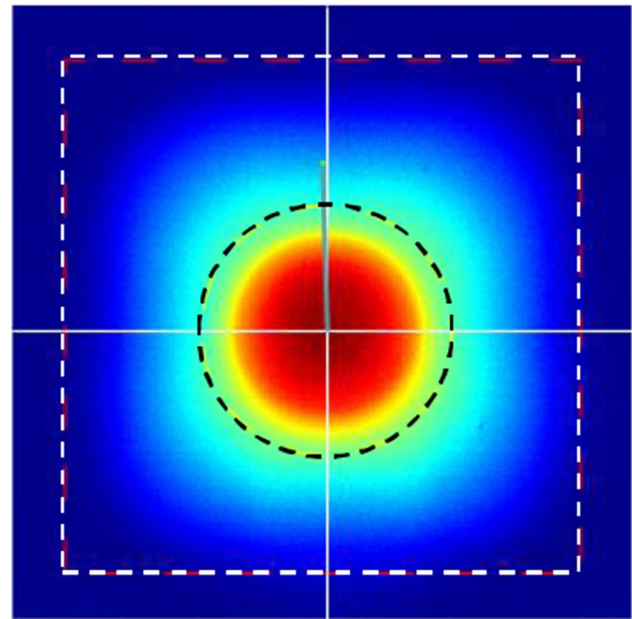


Fig. 3 Example of a laser beam configuration with the VED optic module: inner circular spot (black dashed circle) and outer squared one (white dashed square)

based on the displacement measurements of the movable crosshead rather than on extensometer measurements. Although it gives approximate absolute elongation values since it takes into account also the machine jaws and crosshead deformations, this method was considered more reliable in order to have comparable results between all tensile tests of the experimental campaign. Indeed, failures inside the tensile specimen parallel length (120 mm) but outside the gauge length of the extensometer (87.5 mm) happened affecting the strain measurement comparability with the extensometer for those tests. Nevertheless, beyond the comparison between all DoE configurations, additional tensile tests were carried out in the same conditions but with more precise absolute strain measurements with an extensometer for the most relevant configurations. Ultimate tensile strength (UTS , MPa), elongation to UTS (δ_{UTS} , mm), and elongation to failure (δ_f , mm) results were analyzed in order to evaluate the mechanical behavior of welded joints in a wide range of process parameters. Further metallographic analyses comprising macrographs, hardness tests, and chemical analyses were made on the

Table 3 Levels for each factor of the 3^3 full factorial DoE

	v_W (m/min)	v_W/v_F	Q (J/mm)
Level 1	5.5	1.25	56
Level 2	6.0	1.50	62
Level 3	6.5	1.75	70

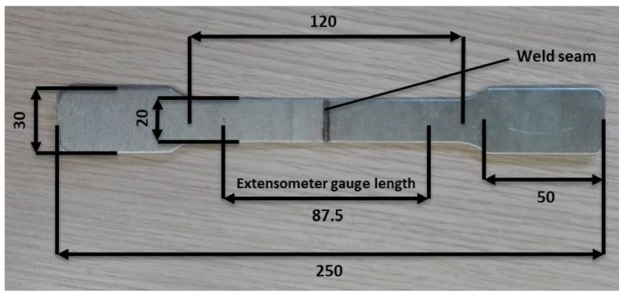


Fig. 4 Tensile specimen from TWB samples with dimensions (mm)

configurations with the best and the worst mechanical results. For all these analyses, cross-sections were cut transversally to the as-quenched weld seam with a precision cutting machine (Struers Secotom-50), mounted with the mounting press Struers CitoPress-30, and then ground and polished with the automatic polisher Struers Tegramin-25. Finally, specimens were etched with a 2% Nital solution for 5–10 s. Cross-sections were observed by the Nikon Eclipse MA200 optical microscope for macro-graphic analysis. High-magnification images and elemental analyses with a secondary electron detector (SED) were conducted on the scanning electron microscope (SEM) with energy dispersive spectroscope (EDS) JEOL JSM-IT500HR, using a landing voltage of 20 kV in high-vacuum mode. SEM–EDS analyses were performed in the most critical zones for the ferrite formation in the FZ for a

total of 5 areas analyzed per cross-section, as schematized in Fig. 5a. Hardness analyses ($HV_{0.5}$) based on three test series of 30 hardness points for each one (i.e., a total of 90 hardness points evaluated for each weld bead section) were conducted on the hardness tester Qness Q30 A+ following the scheme of Fig. 5b.

3 Results and discussion

3.1 Statistical analyses on tensile test results

Figure 6 shows scatterplots related to UTS and elongation results of the tensile testing campaign. The first important consideration is that UTS values are all above 1400 MPa with an average value of 1523 MPa that is much higher than those observed in the literature in as-received welded then hot-stamped (ARWHS) conditions (1129 ± 75 MPa) and aligned with those of hot-stamped base material (HSBM) (1527 ± 26 MPa) [23]. Scatterplots show also a good linear correlation between UTS and elongation values (Pearson correlation coefficient $\rho = 0.75$ between UTS and δ_{UTS} , $\rho = 0.69$ between UTS and δ_f); for this reason, the latter will be neglected in the following analyses for the identification of the most optimal configuration. In Table 4, the process parameters of the experimental plan are reported together with the results of UTS averaged on the three tensile test replications per configuration. Figure 7 shows boxplots of UTS results considering the variations of DoE factors. For all of

Fig. 5 Schemes of position of SEM–EDS investigated areas (upper left (UL), upper right (UR), central zone (C), lower left (LL), lower right (LR)) (a) and hardness test series (b) on a generic cross-section

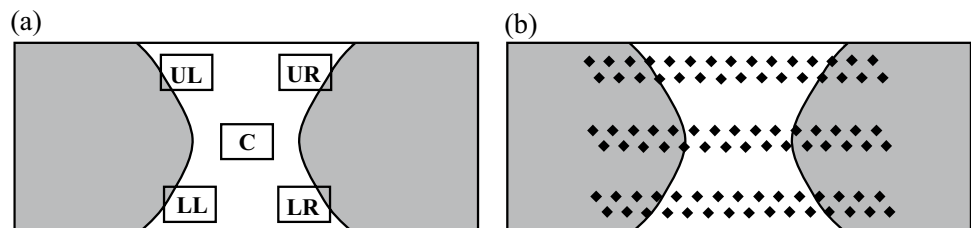
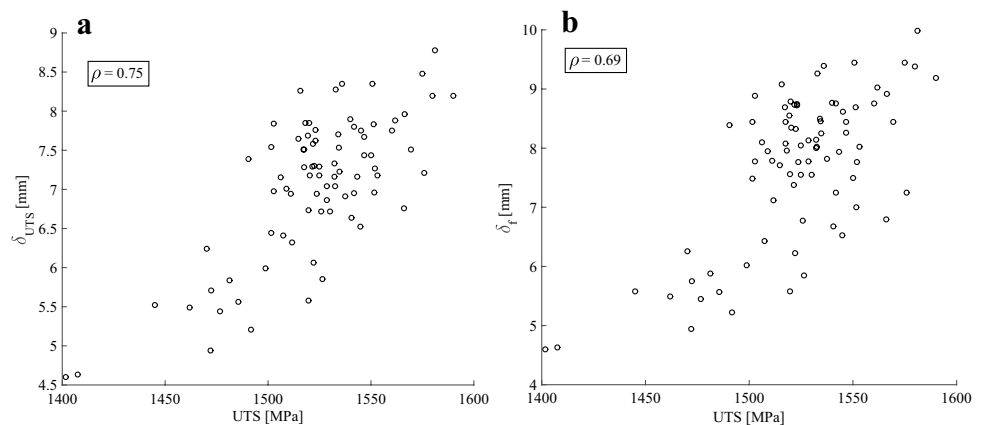


Fig. 6 Scatterplots of tensile tests overall results of $UTS - \delta_{UTS}$ (a) and $UTS - \delta_f$ (b) with related Pearson correlation coefficients ρ



them, no statistically significant differences were registered in *UTS* values considering their variations with a confidence level of 95%. However, the lowest levels of both v_W/v_F and *Q* could be preferable due to the lower scattering and higher repeatability of results. The solutions that registered respectively the highest and the lowest average values of *UTS*, i.e., configurations “O” (1562 MPa) and “E” (1482 MPa), were selected for further analyses. These configurations differ for v_W and *Q* values (both higher for configuration “O”) but maintain the same intermediate level for v_W/v_F .

3.2 Microstructural evolution, macrographs, and SEM–EDS analysis

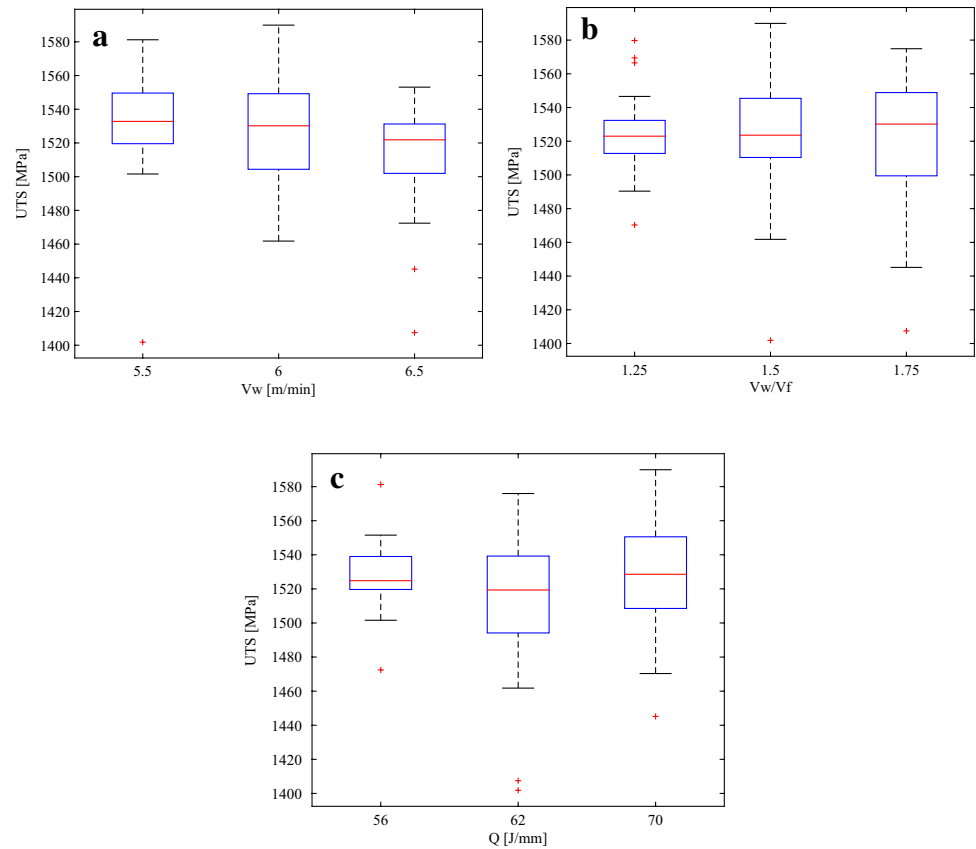
The microstructure of the 22MnB5 steel in the as-received condition is mainly composed of ferrite, pearlite, and a small amount of martensite at the grain boundaries, while the typical morphology of lath martensite can be observed in the hot-stamped condition [27]. The microstructural evolution at the steel-coating interface for Al–Si-coated

22MnB5 has been already extensively studied [50, 51]. The variation of the austenitizing temperature and/or hold time results in a change of the major constituent in the coating from Fe_2Al_5 to a layered structure of FeAl, Fe_3Al , and Fe(Al) and a variation in the thickness of the interdiffusion layer. In particular, the interdiffusion layer considering an austenitizing heat treatment at a temperature of 900 °C for 6.5 min (i.e., condition close to that of this study, and more generally to industrial hot stamping processes) is characterized by α -Fe(Al), Fe_3Al , FeAl, Fe_2Al_5 , and a Fe–Al–Si ternary intermetallic phase [50]. It was already observed that the presence of the Al–Si coating promotes the formation of ferrite into the FZ [23, 25–29]. In particular, the coating mixing is most noticeable along the fusion boundaries, i.e., at the FZ–BM interface, where ferrite was formed as a continuous structure due to the effect of Marangoni convection flow [27, 52, 53]. These comet-shaped segregation zones show a single-phase $Fe_3(Al,Si)$ microstructure and are characterized by high Al concentrations (8.24–15.10 wt.%) in the ARWHS condition [54]. The hot-stamping process can

Table 4 DoE experimental plan

Configuration	v_W (m/min)	v_W/v_F	<i>Q</i> (J/mm)	v_F (m/min)	P_L (kW)	Average <i>UTS</i> (MPa)
A	5.50	1.25	56	4.40	5.13	1520
B	5.50	1.25	62	4.40	5.68	1542
C	5.50	1.25	70	4.40	6.42	1544
D	5.50	1.50	56	3.67	5.13	1540
E	5.50	1.50	62	3.67	5.68	1482
F	5.50	1.50	70	3.67	6.42	1527
G	5.50	1.75	56	3.14	5.13	1532
H	5.50	1.75	62	3.14	5.68	1550
I	5.50	1.75	70	3.14	6.42	1544
J	6.00	1.25	56	4.80	5.60	1518
K	6.00	1.25	62	4.80	6.20	1519
L	6.00	1.25	70	4.80	7.00	1531
M	6.00	1.50	56	4.00	5.60	1536
N	6.00	1.50	62	4.00	6.20	1503
O	6.00	1.50	70	4.00	7.00	1562
P	6.00	1.75	56	3.43	5.60	1533
Q	6.00	1.75	62	3.43	6.20	1536
R	6.00	1.75	70	3.43	7.00	1503
S	6.50	1.25	56	5.20	6.07	1529
T	6.50	1.25	62	5.20	6.72	1501
U	6.50	1.25	70	5.20	7.58	1521
V	6.50	1.50	56	4.33	6.07	1527
W	6.50	1.50	62	4.33	6.72	1505
X	6.50	1.50	70	4.33	7.58	1533
Y	6.50	1.75	56	3.71	6.07	1512
Z	6.50	1.75	62	3.71	6.72	1492
ZZ	6.50	1.75	70	3.71	7.58	1487

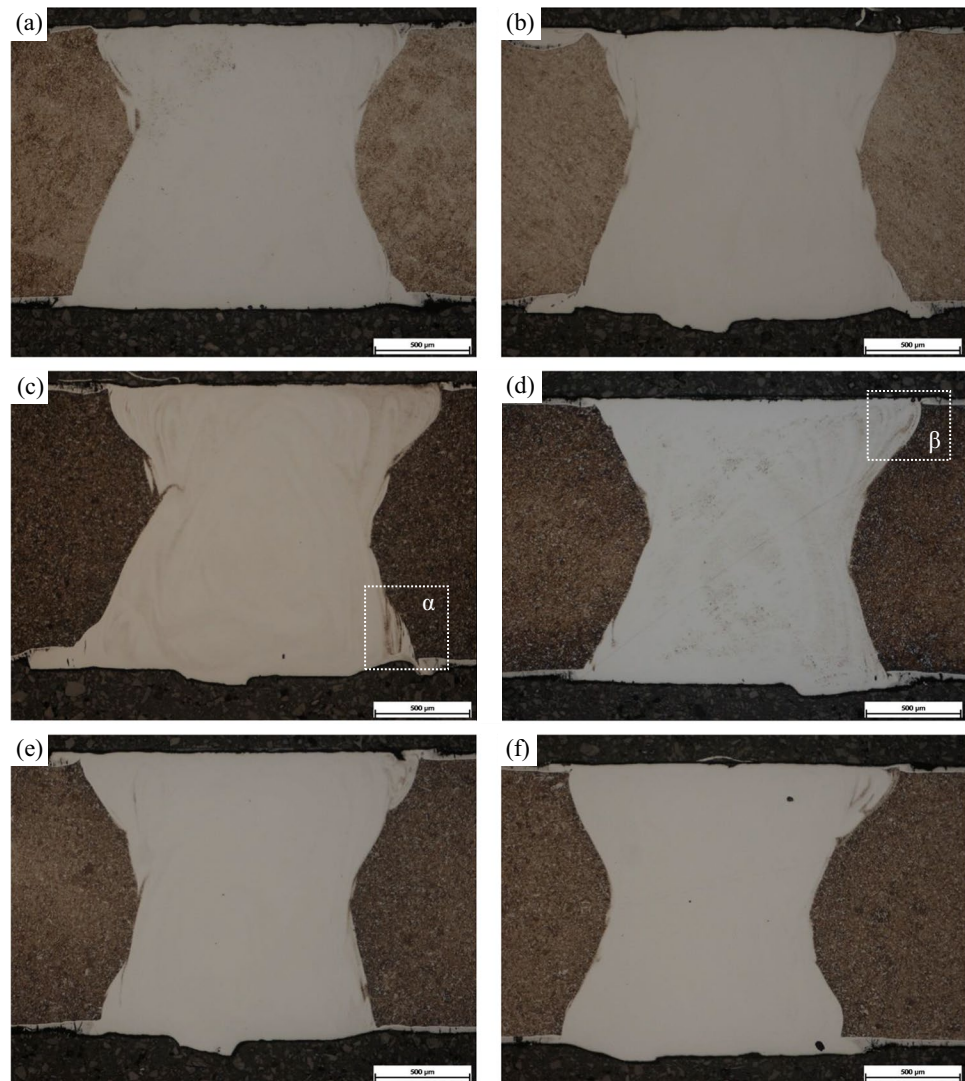
Fig. 7 Boxplots of tensile tests results of *UTS* considering the variations of DoE factors: v_w (a), v_w/v_f (b), Q (c)



cause a change in the microstructure at the fusion boundary from $\text{Fe}_3(\text{Al},\text{Si})$ to a large amount of polygonal ferrite. In addition, the Al from the coating layer is generally distributed unevenly in the FZ, which shows martensite microstructure with bainite in the Al-rich zones. However, the ferrite formation both at the FZ-BM interface and in the FZ in ARWHS condition is clearly due to the relatively high Al contents in the comet-shaped segregation zones at the boundaries [54]. In Fig. 8, cross-section macrographs of each welding replication of configurations “O” (Fig. 8a–c) and “E” (Fig. 8d–f) are reported. Generally, the FZ is characterized by a particular light coloration, which was seen also in welding cross-sections obtained with pure Ni foil/layer [36, 37, 39], thanks to the introduction of the Cr-Ni-composed filler wire. The combined use of the filler wire and the VED laser optics brings wide hourglass-shaped weld sections. Macrographs reveal no substantial differences in cross-section shapes both between replications of the same configuration and between the configurations “O” and “E,” except a generally wider FZ waist of about 0.1 mm due to the higher heat input of the former than the latter. All these cross-sections were further investigated on SEM–EDS. In Figs. 9 and 10, examples of the SEM–EDS analyses conducted respectively on configuration “O” and “E” are reported. Figures 9a and 10a show magnified views of areas indicated in Fig. 8c and d taken into account for

these examples. High-magnification images (Figs. 9b and 10b) display that FZ is characterized by a smooth texture due to the martensite alloyed with filler wire. The FZ-BM interface regions show comet-shaped not-alloyed martensite zones, especially closer to the sheet free surfaces. These zones display the same lath texture of BM and no ferrite was detected in any sample. These results are confirmed by chemical analyses conducted in the same high-magnified areas. Al and Si elemental maps (Figs. 9c, d and 10c, d) prove that the long comet shapes along fusion boundaries are not due to ferrite inclusions because there are no corresponding Al and Si concentrations peaks as observed in the literature [27, 54]. Instead, a lower concentration of both Cr and Ni, i.e., the major chemical components of the filler wire, that reveals its mixing inside FZ, is detected in related elemental maps (Figs. 9e, f and 10e, f) right at comet shapes, demonstrating that these areas correspond to inclusions of BM not homogeneously stirred with the molten filler wire. In addition, complete quantitative chemical compositions of examined areas are listed in Figs. 9g and 10g. Table 5 shows chemical compositions in terms of weight percent averaged on the three replications per configuration. Considering the averages of all the investigated areas, substantially no differences are observed for Al and Si content between the two configurations, registering 0.65% and about 0.40% averaged content of Al and Si, respectively.

Fig. 8 Cross-section macrographs of as-quenched welded joints: configuration “O” (a–c); configuration “E” (d–f)



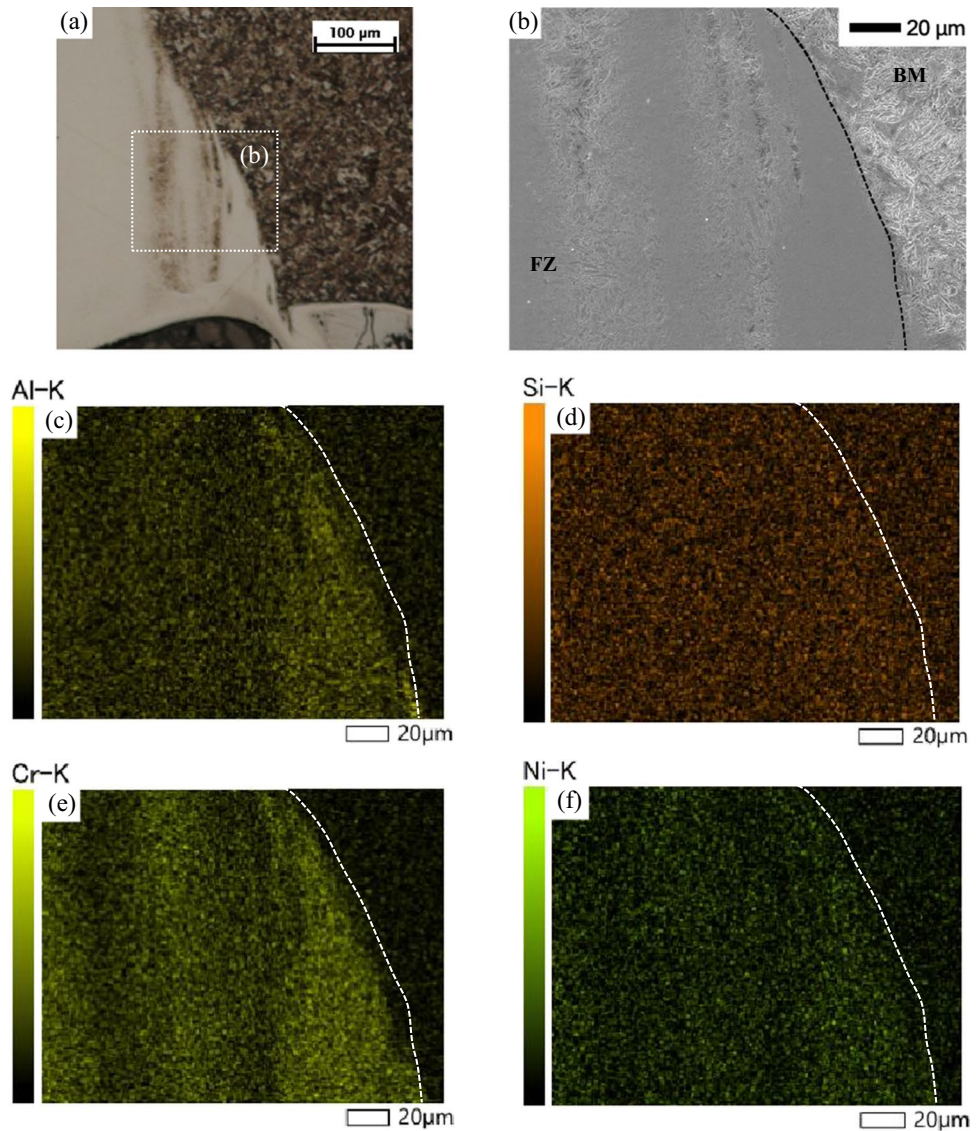
Cr and Ni, introduced almost entirely by the filler wire in the weld pool, are the major alloying elements (3.84% and 1.84% averaged weight content, respectively), and, together with Fe, represent about 98.5% of the mass of the whole FZ. Assuming the weld seam as a Fe–Cr–Ni alloy, the related ternary alloy phase diagram already proposed in the literature [55] shows that the FZ with the element averaged weight content obtained by SEM–EDS analyses is characterized by a full FCC microstructure (i.e., austenite with no ferrite) at a temperature of 850 °C, i.e., above the Ac3 one [56]. However, the use of a ternary alloy phase diagram could not be exhaustive since it does not take into account the effects of other chemical components, i.e., Al, Si, Mn, and C, which have noticeable effects on the FZ microstructure even in little amounts. For this reason, the use of constitution diagrams, such as the Schaeffler or COHMS ones [57, 58], where the Cr and Ni equivalent quantities are calculated considering the presence of other elements with similar effects on the microstructure, could be preferable.

These diagrams confirm that the final microstructure of a FZ with the element averaged weight content obtained by the SEM–EDS analyses of this work is characterized by full martensite. Unfortunately, the use of these constitution diagrams is not recommended for this case since the prediction of the weld metal microstructure can be inaccurate when the cooling rate is high, e.g., in laser beam welding [57–59]. Another empirical calculation of the Cr and Ni equivalent content was used to predict the solidification mode of the Fe–Al–Mn–C weld [60] and employed also for the evaluation of laser-welded Al–Si-coated 22MnB5 steel FZs [28]. Cr and Ni equivalent contents are calculated as follows:

$$\begin{aligned} \text{Cr}_{\text{eq}}(\text{wt.}\%) &= 1[\text{Cr}] + 1[\text{Mo}] + 1.5[\text{Si}] + 5.5[\text{Al}]; \\ \text{Ni}_{\text{eq}}(\text{wt.}\%) &= 1[\text{Ni}] + 30[\text{C}] + 25[\text{N}] + 0.5[\text{Mn}]. \end{aligned}$$

The solidification behaviors of steels are generally categorized into four modes, depending on the ratio $\text{Cr}_{\text{eq}}/\text{Ni}_{\text{eq}}$. The A-mode, i.e., full austenite without ferrite, is obtained

Fig. 9 Magnification of the area α indicated in Fig. 8c, i.e., the LR part of a cross-section macrograph of the configuration “O” (a); SEM micrograph of a more detailed zone (b) with related elemental maps of Al (c), Si (d), Cr (e), and Ni (f), and table of chemical composition (g)



(g)

Element	Line	Mass%	Atom%
C	K	0.22 ± 0.00	1.00 ± 0.00
Al	K	0.51 ± 0.00	1.04 ± 0.00
Si	K	0.36 ± 0.00	0.70 ± 0.00
Cr	K	3.06 ± 0.00	3.22 ± 0.00
Mn	K	1.26 ± 0.00	1.25 ± 0.00
Fe	K	93.11 ± 0.03	91.39 ± 0.02
Ni	K	1.48 ± 0.01	1.38 ± 0.00
Total		100.00	100.00

when $Cr_{eq}/Ni_{eq} < 1.25$. This is the case of this study since $Cr_{eq}/Ni_{eq} < 0.90$ for all the SEM–EDS-analyzed weld seams. Generally, the results of predictive methods could be affected by FZ chemical compositions, heating and cooling rates, and influences of particular elements on phase diagrams. For these reasons, the experimental results of the hardness and tensile tests reported in the following subsection are to be considered the main proof of the absence of ferrite in the FZ microstructure together with SEM–EDS analyses. It

was already observed that the filler wire method causes an enhanced stirring of the melt pool, improving the homogeneity of Al distribution inside the FZ and bringing to a more uniform ferrite distribution [31]. In addition, a high-carbon content of filler wire could act as an austenite stabilizer, suppressing ferrite formation and improving martensite fraction in the hot-stamping heat-treated weld seam [32]. Moreover, laser welding with larger laser spots allows a wider melt pool with enhanced flows that improve the Al mixing leading to

Fig. 10 Magnification of the area β indicated in Fig. 8d, i.e., the UR part of a cross-section macrograph of the configuration “E” (a); SEM micrograph of a more detailed zone (b) with related elemental maps of Al (c), Si (d), Cr (e), and Ni (f), and table of chemical composition (g)

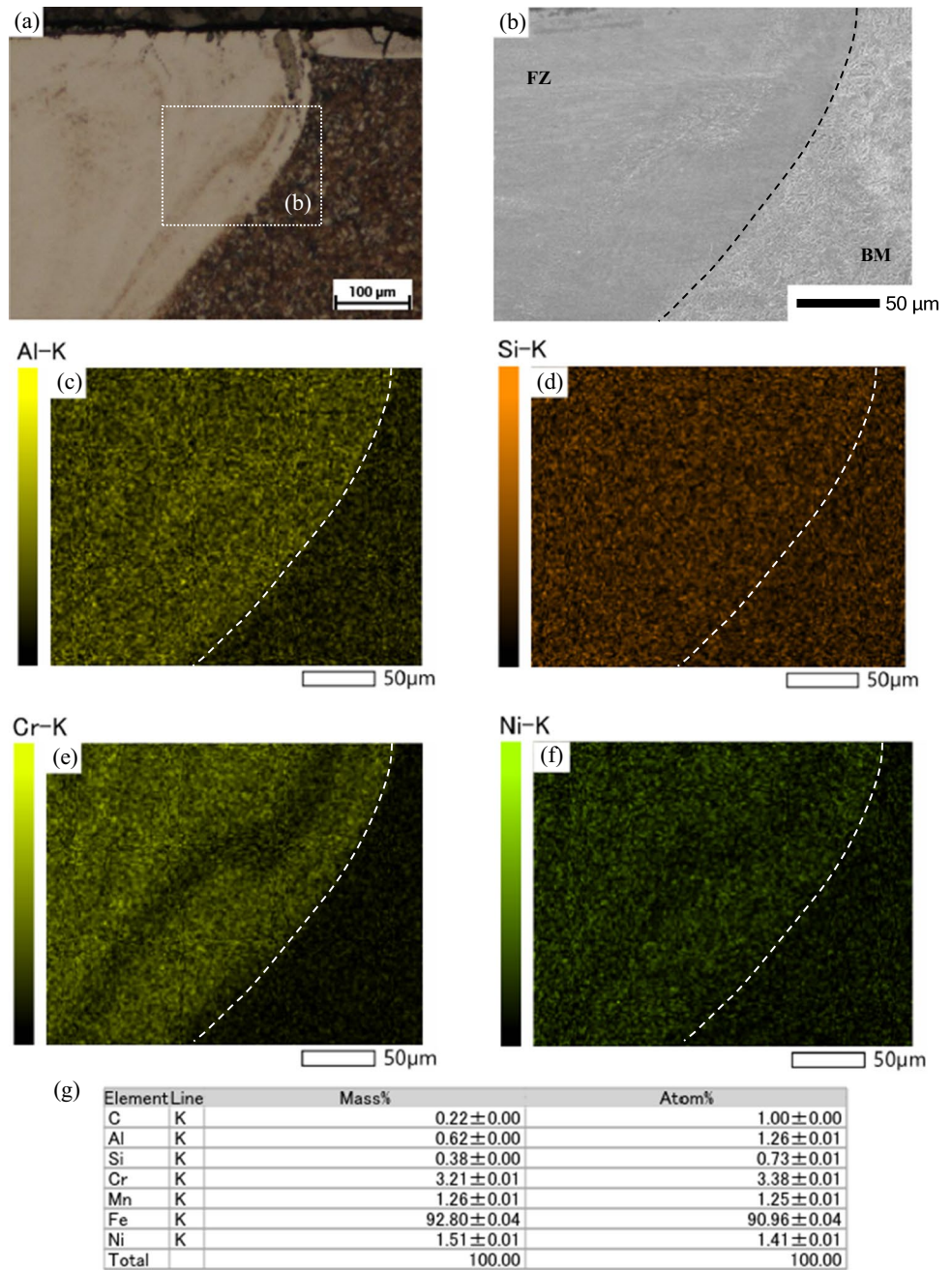


Table 5 Chemical compositions with averaged values per investigated area calculated from EDS analyses of 3 different as-quenched welded joints per configuration

Element (wt.%)	Configuration	Al		Si		Cr		Ni	
		O	E	O	E	O	E	O	E
Investigated area	Upper left	0.65	0.59	0.38	0.40	3.31	4.49	1.56	2.15
	Upper right	0.69	0.61	0.37	0.37	2.69	2.76	1.27	1.30
	Center	0.73	0.78	0.43	0.43	4.84	4.85	2.31	2.32
	Lower left	0.62	0.69	0.40	0.42	4.34	4.74	2.10	2.29
	Lower right	0.57	0.58	0.36	0.37	2.93	3.39	1.43	1.63
	Overall average	0.65	0.65	0.39	0.40	3.62	4.05	1.74	1.94

an increased martensitic fraction in the FZ after hot stamping [44]. Therefore, it is expected that the combined use of filler wire and VED optic module (which could be assumed a laser spot enlarging method) brings to much more enhanced stirring effects of the melt pool than those observed for each of the two methods employed separately. A detailed evaluation of these events is quite difficult since keyhole laser welding is a complex multi-physical problem involving several physical phenomena such as laser–material interaction, conduction, melting, vaporization, plasma generation, fluid flow, and surface deformation. This topic is currently under investigation through numerical modeling and will be detailed in further studies.

3.3 Mechanical properties

Figure 11 shows the results of hardness tests conducted on samples of configurations “O” and “E.” For both configurations, hardness values are included in the range 494–543 HV_{0.5}, which are aligned with the typical values for the 22MnB5 HSBM (500–550 HV) [23]. In previous studies, significant drops of hardness of about 40% compared

to the BM are detected in the FZ due to the presence of softer ferrite [27, 28, 39, 41]. In this case, the comparison between BM and FZ hardness values highlights variations lower than 5% thanks to the martensitic microstructure of the weld seam. In addition, no significant differences can be found between the two configurations. Figure 12 reports the tensile curves obtained from the tests conducted with more precise absolute strain measurements carried out with an extensometer. An example of both the configurations “O” and “E” is depicted. For the configuration “O,” a UTS value of 1567 MPa and a total elongation of 5.35% were registered, while the sample of configuration “E” performed 1494 MPa for UTS and 4.90% of total elongation. These results confirm those obtained in the comparison between DoE configurations described before and are substantially aligned with the same observed for HSBM [23]. As observed for hardness values, no significant drops of UTS and total elongation values are observed as in other cases with ferritic FZ microstructures [27, 28, 39, 41]. This confirms one more time the absence of softer ferrite in the weld seam.

Fig. 11 HV_{0.5} hardness distribution of up (blue circles), central (black squares), and bottom (red asterisks) series across the weld section of configuration “O” (a) and configuration “E” (b) with BM/FZ zone limiters for each series (dashed lines colored as the respective series)

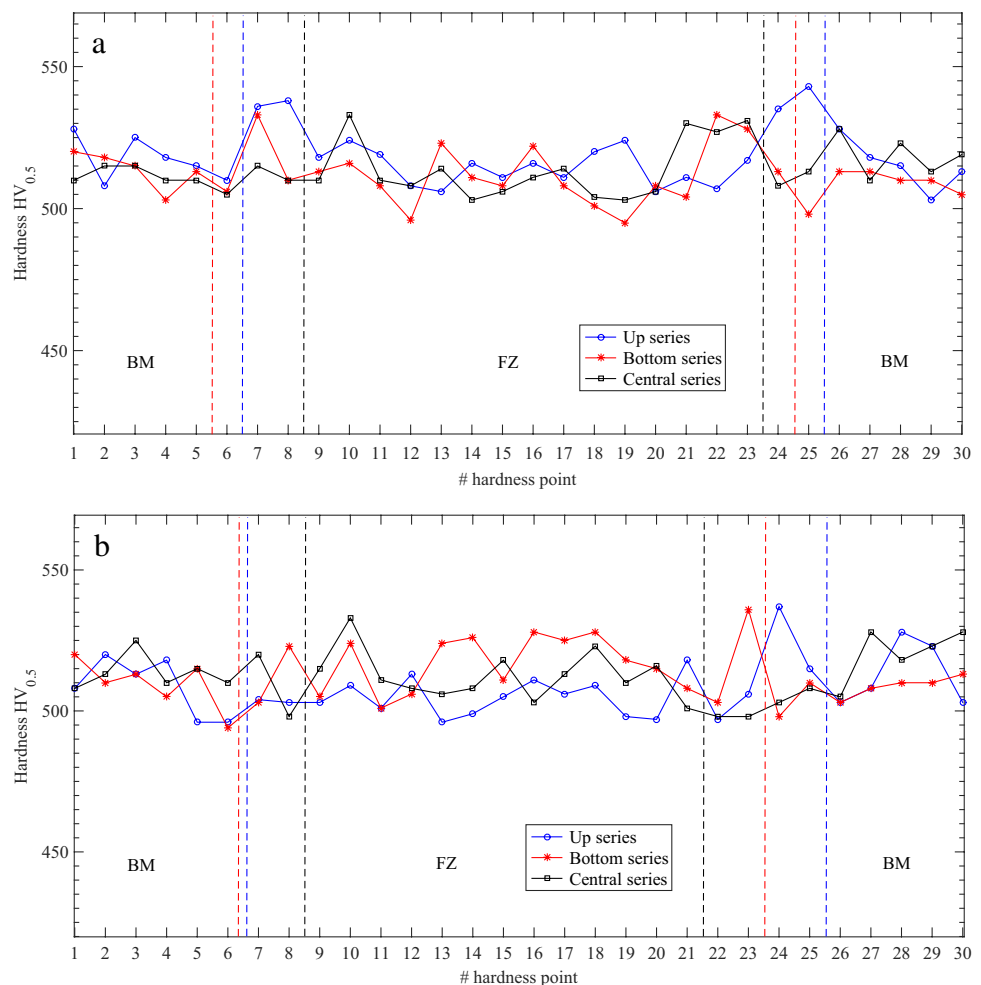
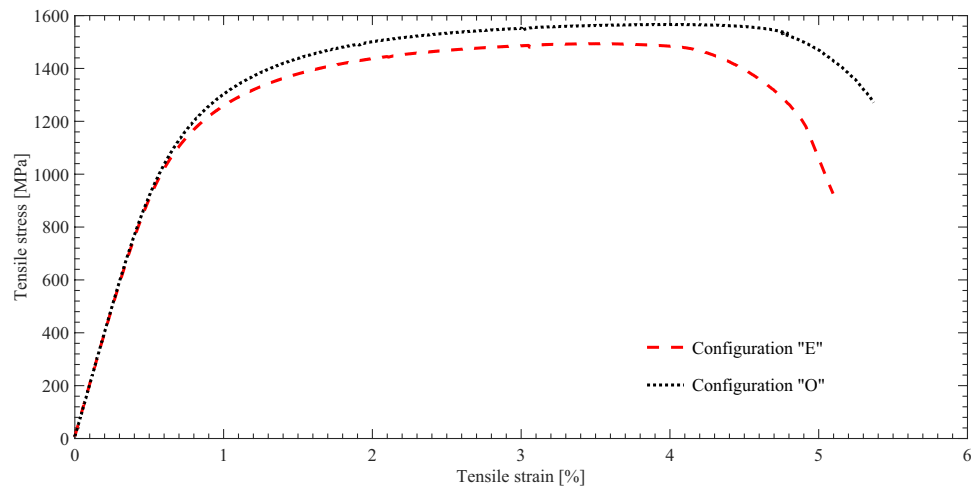


Fig. 12 Examples of tensile curves of configuration “E” (red dashed line) and configuration “O” (black dotted line) butt joints, all in hot-stamped conditions



4 Conclusions

In this work, a novel approach for laser welding of Al-Si-coated 22MnB5 steel for hot stamping considering the use of both a filler wire and a variable energy distribution laser optics has been developed and investigated. *UTS* values from a 3^3 full factorial DoE experimental plan have been all above 1400 MPa, with an average value of 1523 MPa that is much higher than those observed in as-received welded then hot-stamped attempts and aligned to hot-stamped base material ones. No statistically significant differences in *UTS* values have been registered considering variations of DoE factors, i.e., the main process parameters. Wide hourglass-shaped weld seam has been observed in cross-section macrographs. SEM high-magnification images have shown the smooth texture of the fusion zone due to the martensite alloyed with filler wire, and the presence of comet-shaped not-alloyed martensite zones at the interface regions with the same lath texture of the base material. EDS analyses have demonstrated that these comet shapes are not due to ferrite inclusions because no corresponding Al and Si concentration peaks have been observed, but they represent inclusions of the base material not homogeneously stirred with the molten filler wire. In addition, the overall weight averaged content of Al and Si inside the fusion zone is about 0.65% and 0.40%, respectively. Hardness tests have registered values in the range of 494–543 HV_{0.5} that are aligned with those of hot-stamped base material also inside the fusion zone, i.e., no drops of hardness due to the presence of softer ferrite have been detected. Tensile tests with extensometer registered *UTS* values of 1567 and 1494 MPa, with total elongations of 5.35% and 4.90%, respectively, confirming the strength performances obtained in the DoE. The wide experimental campaign conducted in this work has proven that this laser welding process is very stable and reliable thanks to the good results obtained in the most critical configuration for a TWB (joining of the same materials with the same thicknesses) and even with slight variations of the main

process parameters. The latter could be intended as the representative case of a typical production process where little alterations of optimal process parameters due to unexpected events could arise. In addition, the adduced simplification of the entire production process of TWB for hot stamping obtained avoiding any additional decoating step should be considered. For these reasons, the proposed welding methodology is in the running to be a valid alternative to laser ablation procedures thanks to its particular suitability for industrial applications.

Funding Open access funding provided by Università degli Studi della Basilicata within the CRUI-CARE Agreement. The research reported in this work was partially funded by the Italian Ministry of Economic Development (Project AtaBHot Cup n. B88I17001090008).

Declarations

Ethics approval This manuscript is the authors' own original work, which has not been previously published elsewhere. The manuscript is not currently being considered for publication elsewhere. The manuscript reflects the authors' own research and analysis in a truthful and complete manner.

Consent for publication The authors give their consent for the publication of the manuscript.

Conflict of interest The authors declare no competing interests.

Open Access This article is licensed under a Creative Commons Attribution 4.0 International License, which permits use, sharing, adaptation, distribution and reproduction in any medium or format, as long as you give appropriate credit to the original author(s) and the source, provide a link to the Creative Commons licence, and indicate if changes were made. The images or other third party material in this article are included in the article's Creative Commons licence, unless indicated otherwise in a credit line to the material. If material is not included in the article's Creative Commons licence and your intended use is not permitted by statutory regulation or exceeds the permitted use, you will need to obtain permission directly from the copyright holder. To view a copy of this licence, visit <http://creativecommons.org/licenses/by/4.0/>.

References

- Merklein M, Johannes M, Lechner M, Kuppert A (2014) A review on tailored blanks – production, applications and evaluation. *J Mater Process Technol* 214:151–164. <https://doi.org/10.1016/j.jmatprotec.2013.08.015>
- Kumar A, Gautam V (2021) Formability of tailor welded blanks of high strength steel: a review. *Mater Today Proc.* <https://doi.org/10.1016/j.matpr.2021.04.016>
- Cheah LW, Heywood JB (2010) Cars on a diet: the material and energy impacts of passenger vehicle weight reduction in the U.S. <https://dspace.mit.edu/handle/1721.1/62760>. Accessed 24 Jan 2023
- Redelbach M, Klötzke M, Friedrich HE (2012) Impact of light-weight design on energy consumption and cost effectiveness of alternative powertrain concepts. *Eur Electr Veh Congr* 19–22 Nov 2012, Brussels, Belgium. <https://elib.dlr.de/80771/>. Accessed 24 Jan 2023
- Del Pero F, Berzi L, Antonacci A, Delogu M (2020) Automotive lightweight design: simulation modeling of mass-related consumption for electric vehicles. *Machines* 8. <https://doi.org/10.3390/machines8030051>
- Joost WJ (2012) Reducing vehicle weight and improving U.S. energy efficiency using integrated computational materials engineering. *JOM* 64:1032–1038. <https://doi.org/10.1007/s11837-012-0424-z>
- Lutsey N (2012) Regulatory and technology lead-time: the case of US automobile greenhouse gas emission standards. *Transp Policy* 21:179–190. <https://doi.org/10.1016/j.tranpol.2012.03.007>
- Zadpoor AA, Sinke J, Benedictus R (2007) Mechanics of tailor welded blanks: an overview. *Key Eng Mater* 344:373–382. <https://doi.org/10.4028/www.scientific.net/KEM.344.373>
- ArcelorMittal (2018) Lightweighting with laser-welded blanks. In: *Automot. Manuf. Solut.* <https://www.automotivemanufacturing.com/materials/lightweighting-with-laser-welded-blanks/36344.article>. Accessed 29 Sep 2021
- Duque Múnica D, Pic A, Abou-Khalil D, et al (2008) Innovative press hardened steel based laser welded blanks solutions for weight savings and crash safety improvements. *SAE Int J Mater Manuf* 1:2008-01-1076. <https://doi.org/10.4271/2008-01-1076>
- Keeler S, Kimchi M, Mooney PJ (2017) Advanced high-strength steels guidelines version 6.0. WorldAutoSteel. http://www.worldautosteel.org/download_files/AHSS%20Guidelines%20V6/00_AHSSGuidelines_V6_20170430.pdf. Accessed 24 Jan 2023
- Huetter J (2018) Ducker research: autos lost 153.9 lbs of mild steel since 2013, traded up to tougher grades. <https://www.repairerdrivenews.com/2018/07/31/ducker-research-cars-lost-153-9-lbs-of-mild-steel-since-2013-traded-up-to-tougher-grades/>. Accessed 8 Oct 2021
- Kleiner M, Geiger M, Klaus A (2003) Manufacturing of light-weight components by metal forming. *CIRP Ann Manuf Technol* 52:521–542. [https://doi.org/10.1016/S0007-8506\(07\)60202-9](https://doi.org/10.1016/S0007-8506(07)60202-9)
- Graf A (2021) Aluminum alloys for lightweight automotive structures. In: *Materials, design and manufacturing for lightweight vehicles*. Elsevier, pp 97–123. <https://doi.org/10.1016/B978-0-12-818712-8.00003-3>
- Hakamada M, Furuta T, Chino Y et al (2007) Life cycle inventory study on magnesium alloy substitution in vehicles. *Energy* 32:1352–1360. <https://doi.org/10.1016/j.energy.2006.10.020>
- Mayyas AT, Qattawi A, Mayyas AR, Omar MA (2012) Life cycle assessment-based selection for a sustainable lightweight body-in-white design. *Energy* 39:412–425. <https://doi.org/10.1016/J.ENERGY.2011.12.033>
- Li Z, Rostam K, Panjehpour A et al (2020) Experimental and numerical study of temperature field and molten pool dimensions in dissimilar thickness laser welding of Ti6Al4V alloy. *J Manuf Process* 49:438–446. <https://doi.org/10.1016/j.jmapro.2019.11.024>
- Nguyen Q, Azadkhou A, Akbari M et al (2020) Experimental investigation of temperature field and fusion zone microstructure in dissimilar pulsed laser welding of austenitic stainless steel and copper. *J Manuf Process* 56:206–215. <https://doi.org/10.1016/j.jmapro.2020.03.037>
- Naganathan A, Penter L (2012) Hot stamping. In: *Sheet metal forming*. ASM International, pp 133–156. <https://doi.org/10.31399/asm.tb.smfpa.t53500133>
- Billur E (2019) Hot stamping of ultra high-strength steels. Springer International Publishing, Cham
- Karbasian H, Tekkaya AE (2010) A review on hot stamping. *J Mater Process Technol* 210:2103–2118. <https://doi.org/10.1016/j.jmatprotec.2010.07.019>
- Fan DW, De Cooman BC (2012) State-of-the-knowledge on coating systems for hot stamped parts. *Steel Res Int* 83:412–433. <https://doi.org/10.1002/srin.201100292>
- Khan MS, Razmpoosh MH, Biro E, Zhou Y (2020) A review on the laser welding of coated 22MnB5 press-hardened steel and its impact on the production of tailor-welded blanks. *Sci Technol Weld Join* 25:447–467. <https://doi.org/10.1080/13621718.2020.1742472>
- Geng Y, Akbari M, Karimipour A et al (2019) Effects of the laser parameters on the mechanical properties and microstructure of weld joint in dissimilar pulsed laser welding of AISI 304 and AISI 420. *Infrared Phys Technol* 103:103081. <https://doi.org/10.1016/j.infrared.2019.103081>
- Kim C, Kang MJ, Park YD (2011) Laser welding of Al-Si coated hot stamping steel. *Procedia Eng* 10:2226–2231. <https://doi.org/10.1016/j.proeng.2011.04.368>
- Moon JH, Seo PK, Kang CG (2013) A study on mechanical properties of laser-welded blank of a boron sheet steel by laser ablation variable of Al-Si coating layer. *Int J Precis Eng Manuf* 14:283–288. <https://doi.org/10.1007/s12541-013-0039-5>
- Saha DC, Biro E, Gerlich AP, Zhou YN (2016) Fiber laser welding of AlSi coated press hardened steel. *Weld J* 95:147–156
- Lin W, Li F, Wu D et al (2018) Effect of Al-Si coating on weld microstructure and properties of 22MnB5 steel joints for hot stamping. *J Mater Eng Perform* 27:1825–1836. <https://doi.org/10.1007/s11665-018-3259-0>
- Yang H, Sun Y, Tan C et al (2020) Influence of Al-Si coating on microstructure and mechanical properties of fiber laser welded and then press-hardened 22MnB5 steel. *Mater Sci Eng A* 794:139918. <https://doi.org/10.1016/j.msea.2020.139918>
- Vierstraete R, Ehling W, Pinard F et al (2010) Laser ablation for hardening laser welded steel blanks. In: *Ind. Laser Solut.* <https://www.industrial-lasers.com/surface-treatment/article/16489496/laser-ablation-for-hardening-laser-welded-steel-blanks>. Accessed 8 Oct 2021
- Lin W, Li F, Hua X, Wu D (2018) Effect of filler wire on laser welded blanks of Al-Si-coated 22MnB5 steel. *J Mater Process Technol* 259:195–205. <https://doi.org/10.1016/j.jmatprotec.2018.04.041>
- Lee CW, Kim SY, Jang SG et al (2019) Fusion zone microstructural evolution of Al-10% Si coated hot stamping steel during laser welding. *ISIJ Int* 59:136–143. <https://doi.org/10.2355/isijinternational.ISIJINT-2018-489>
- Zhou L, Zhu C, Ma R, Wei Z (2021) Research on parameters of wire-filling laser welding and quenching process for joints microstructure and mechanical property of BR1500HS steel. *Metals (Basel)* 11:1047. <https://doi.org/10.3390/met11071047>
- Breuer A, Both C (2017) Laser welding method for producing a semi-finished sheet metal product from hardenable steel, comprising an aluminum- or aluminum-silicon-based coating. <https://doi.org/10.1016/j.jmapro.2017.03.001>

- patents.google.com/patent/WO2017050711A1/en. Accessed 24 Jan 2023
35. Both C, Heydt J von der (2017) Trends in welding technology for hotform tailored blank applications. In: International Automotive Body Congress (IABC) 14–15 Jun 2017, Frankfurt, Germany
 36. Sun Q, Di H-S, Wang X-N, Chen X-M (2019) Suppression of δ -ferrite formation on Al-Si coated press-hardened steel during laser welding. *Mater Lett* 245:106–109. <https://doi.org/10.1016/j.matlet.2019.02.111>
 37. Chen X, Wang X, Sun Q et al (2020) Improving the mechanical properties of PHS laser welded joints by adding Ni foil to suppress δ -ferrite. *J Mater Res Technol* 9:5184–5193. <https://doi.org/10.1016/j.jmrt.2020.03.035>
 38. Wang X, Zhang Z, Hu Z et al (2020) Effect of Ni foil thickness on the microstructure of fusion zone during PHS laser welding. *Opt Laser Technol* 125:106014. <https://doi.org/10.1016/j.optlastec.2019.106014>
 39. Shehryar Khan M, Biro E, Zhou Y, Macwan A (2021) α -Ferrite suppression during fiber laser welding of Al-Si coated 22MnB5 press-hardened steel. *Weld J* 100:213–220. <https://doi.org/10.29391/2021.100.018>
 40. Wang Q, Lin W, Li F et al (2021) Influence of thermal modification on Al-Si coating of hot-stamped 22MnB5 steel: microstructure, phase transformation, and mechanical properties. *J Shanghai Jiaotong Univ*. <https://doi.org/10.1007/s12204-021-2267-7>
 41. Khan MS, Razmpoosh MH, Macwan A et al (2021) Optimizing weld morphology and mechanical properties of laser welded Al-Si coated 22MnB5 by surface application of colloidal graphite. *J Mater Process Technol* 293:117093. <https://doi.org/10.1016/j.jmatprotec.2021.117093>
 42. Saha D, Biro E, Gerlich AP, Khan MS (2021) Pre-coated steel sheet comprising an additional coating for increasing the mechanical strength of the weld metal zone of a welded steel part prepared from said pre-coated sheet. https://www.researchgate.net/publication/353265545_Pre-Coated_Steel_Sheet_Comprising_an_Additional_Coating_for_Increasing_The_Mechanical_Strength_of_the_Weld_Metal_Zone_of_a_Welded_Steel_Part_Prepared_From_Said_Pre-Coated_Sheet. Accessed 24 Jan 2023
 43. Shehryar Khan M, Shahabad SI, Yavuz M et al (2021) Numerical modelling and experimental validation of the effect of laser beam defocusing on process optimization during fiber laser welding of automotive press-hardened steels. *J Manuf Process* 67:535–544. <https://doi.org/10.1016/j.jmapro.2021.05.006>
 44. Kang M, Kim YM, Kim C (2016) Effect of heating parameters on laser welded tailored blanks of hot press forming steel. *J Mater Process Technol* 228:137–144. <https://doi.org/10.1016/j.jmatprotec.2015.06.028>
 45. Sun Y, Wu L, Tan C et al (2019) Influence of Al-Si coating on microstructure and mechanical properties of fiber laser welded 22MnB5 steel. *Opt Laser Technol* 116:117–127. <https://doi.org/10.1016/j.optlastec.2019.03.024>
 46. Xu W, Yang S, Tao W et al (2022) Effects of laser beam oscillation welding parameters on Al-Si coated 22MnB5 weld joint properties. *Opt Laser Technol* 149:107898. <https://doi.org/10.1016/j.optlastec.2022.107898>
 47. Wan Z, Wang H-P, Li J et al (2022) Effect of beam oscillation frequency on spattering in remote laser stitch welding of thin-gage zinc-coated steel with keyhole penetration. *J Mater Process Technol* 302:117482. <https://doi.org/10.1016/j.jmatprotec.2021.117482>
 48. Lin W, Li F, Hua X (2018) Effect of keyhole mode on weld shape and mechanical properties of thin sheets of Al-Si coated 22MnB5 steel. *J Laser Appl* 30:042001. <https://doi.org/10.2351/1.5052155>
 49. Krasnoperov MY, Pieters RRG, Richardson IM (2004) Weld pool geometry during keyhole laser welding of thin steel sheets. *Sci Technol Weld Join* 9:501–506. <https://doi.org/10.1179/136217104225021733>
 50. Cho L, Golem L, Seo EJ et al (2020) Microstructural characteristics and mechanical properties of the Al-Si coating on press hardened 22MnB5 steel. *J Alloys Compd* 846:156349. <https://doi.org/10.1016/j.jallcom.2020.156349>
 51. Windmann M, Röttger A, Theisen W (2013) Phase formation at the interface between a boron alloyed steel substrate and an Al-rich coating. *Surf Coat Technol* 226:130–139. <https://doi.org/10.1016/j.surfcoat.2013.03.045>
 52. Limmaneevichitr C, Kou S (2000) Experiments to simulate effect of Marangoni convection on weld pool shape. *Weld J (Miami, Fla)* 79:231s–237s
 53. Limmaneevichitr C, Kou S (2000) Visualization of Marangoni convection in simulated weld pools. *Weld J (Miami, Fla)* 79:126s
 54. Yoon T-J, Oh M-H, Shin H-J, Kang C-Y (2017) Comparison of microstructure and phase transformation of laser-welded joints in Al-10wt%Si-coated boron steel before and after hot stamping. *Mater Charact* 128:195–202. <https://doi.org/10.1016/j.matchar.2017.02.007>
 55. Ben-Artzy A, Reichardt A, Borgonia J-P et al (2021) Compositionally graded SS316 to C300 Maraging steel using additive manufacturing. *Mater Des* 201:109500. <https://doi.org/10.1016/j.matdes.2021.109500>
 56. Çavuşoğlu O, Çavuşoğlu O, Yılmazoğlu AG et al (2020) Microstructural features and mechanical properties of 22MnB5 hot stamping steel in different heat treatment conditions. *J Mater Res Technol* 9:10901–10908. <https://doi.org/10.1016/j.jmrt.2020.07.043>
 57. Lee S, Lee C-Y, Lee Y-K (2015) Schaeffler diagram for high Mn steels. *J Alloys Compd* 628:46–49. <https://doi.org/10.1016/j.jallcom.2014.12.134>
 58. Wittig B, Zinke M, Jüttner S, Keil D (2019) A new constitution diagram for dissimilar metal welds of high-manganese steels. *Weld World* 63:491–499. <https://doi.org/10.1007/s40194-018-0668-5>
 59. Kou S (2002) *Welding metallurgy*. Wiley, Hoboken
 60. Lee C-Y, Lee Y-K (2014) The solidification mode of Fe-Mn-Al-C lightweight steel. *JOM* 66:1794–1799. <https://doi.org/10.1007/s11837-014-1000-5>

Publisher's note Springer Nature remains neutral with regard to jurisdictional claims in published maps and institutional affiliations.